Dalton Transactions

ROYAL SOCIETY OF CHEMISTRY

PAPER

View Article Online
View Journal | View Issue

Cite this: *Dalton Trans.*, 2020, **49**, 11010

Engineering Z-scheme TiO_2-OV-BiOCl *via* oxygen vacancy for enhanced photocatalytic degradation of imidacloprid†

Bin Yang,[a] Jiliang Zheng,[b] Wei Li,[c] Rongjie Wang,[a] Danya Li,[a] Xuhong Guo,[a] Raul D. Rodriguez[d] and Xin Jia*[a]

Received 15th June 2020,
Accepted 19th July 2020

DOI: 10.1039/d0dt02128h

rsc.li/dalton

The development and application of photocatalysts with strong redox ability to degrade refractory pesticides is the key to eliminating pesticide contamination. In this work, we develop a facile, time-saving, and surfactant-assisted method to fabricate a new Z-scheme heterojunction based on TiO_2/BiOCl. This photocatalyst is rich in oxygen vacancy defects (TiO_2-OV-BiOCl), and displays an excellent photocatalytic degradation performance for imidacloprid (IMD), and a possible degradation pathway of IMD is provided. The surfactant F127 plays an essential role in regulating the oxygen vacancy defects (OVDs) of TiO_2-OV-BiOCl, where the OVD mainly exists in 5 layer BiOCl ultrathin nanosheets. Free radical trapping experiments demonstrate that the introduction of an OVD in BiOCl as a 'charge mediator' changes the charge-transfer mode from a type-II mechanism to a Z-scheme mechanism. The formation of a Z-scheme heterojunction leads to an excellent light utilization and higher separation efficiency of photogenerated charge carriers with a prolonged lifetime compared to those of BiOCl and TiO_2/BiOCl. This work highlights the critical role of an OVD in the construction of a Z-scheme heterojunction of TiO_2/BiOCl, and it can be applied to construct efficient photocatalytic systems for pesticide degradation.

1. Introduction

Due to the fast growth of the global population, pesticides are over-applied to increase the yield of crops and meet the increasing worldwide demand for food supply. Because of their high stability and difficult decomposition plus indiscriminate overuse, pesticides pervade in the environment threatening the health of human beings and animals.[1–3] Various methods are being developed to eliminate pesticide contamination, including photocatalysis, electrocatalysis, photoelectric catalysis, and chemical catalytic oxidation (hydrogen peroxide, ozone, and persulfate).[4–8] Among these strategies, photocatalysis is the most promising one for the degradation of pesticides, because photocatalysis is an efficient, energy-smart, low-cost, and repeatable strategy that also generates fewer or non-polluted catabolites.[9–11] However, some pesticides with stable structures, such as imidacloprid (IMD), are difficult to degrade by photocatalysis. Therefore, the development of highly efficient photocatalyst systems to remove IMD contamination is still a significant challenge to overcome.

Bismuth oxychloride (BiOCl) is widely used in the degradation of organic pollutants due to its strong oxidation ability.[12–14] BiOCl is one of the promising candidates for the photocatalytic degradation of IMD. However, the low light absorption and incidental interior recombination caused by its wide bandgap and blocky structure seriously compromise its photocatalytic degradation performance.[15,16] Constructing a heterojunction for BiOCl ultrathin nanosheets could satisfactorily resolve the above shortcomings.[17–19] Recently, Guerrero *et al.* reported that combining TiO_2 with BiOCl can result in excellent stability, increase light utilization, and promote the separation efficiency of photogenerated charges. These characteristics resulting from combining these two oxides ultimately provide a better photocatalytic degradation performance than when using BiOCl and TiO_2 alone.[20] In a TiO_2/BiOCl heterojunction composed of TiO_2 and BiOCl, the photogenerated electrons located in the conduction band (CB) of TiO_2 migrate to the CB of BiOCl. At the same time, the photogenerated holes located in the valence band (VB) of BiOCl migrate to the

[a]*School of Chemistry and Chemical Engineering/Key Laboratory for Green Processing of Chemical Engineering of Xinjiang Bingtuan, Key Laboratory of Materials-Oriented Chemical Engineering of Xinjiang Uygur Autonomous Region, Engineering Research Center of Materials-Oriented Chemical Engineering of Xinjiang Bingtuan, Shihezi University, Shihezi 832003, People's Republic of China. E-mail: jiaxin@shzu.edu.cn*
[b]*Xinjiang Xin Lian Xin Energy Chemical Co., Ltd, China*
[c]*Chair of Macromolecular Chemistry, Faculty of Chemistry and Food Chemistry, School of Science, Technische Universitat Dresden, 01069 Dresden, Germany*
[d]*Tomsk Polytechnic University, 30 Lenin Avenue, 634050 Tomsk, Russia*

†Electronic supplementary information (ESI) available. See DOI: 10.1039/D0DT02128H

VB of TiO_2. This is known as the type-II mechanism.[20–26] This charge-transfer pathway reduces the redox potentials, thus compromising the process of rapid degradation and mineralization of refractory pollutants. Unlike the type-II mechanism, the Z-scheme mechanism not only promotes light absorption and prolongs the lifetime of the photogenerated charge carriers but also maintains strong redox potentials, which is an effective strategy to achieve a high photocatalytic degradation performance.[27,28] The formation of a Z-scheme heterojunction usually requires the assistance of 'charge mediators' that can provide electron and hole transfer centers. Many materials can be used as charge mediators, for example, metal nanoparticles,[29–31] semiconductors,[32] carbon materials,[33,34] *etc*. Compared with these charge mediators for constructing a Z-scheme heterojunction, oxygen vacancy defects (OVDs) as charge mediators have unique advantages without introducing other extraneous materials.[34–37] When an OVD is introduced into TiO_2/BiOCl, it may serve as a charge mediator, changing the charge-transfer mode from a type-II to a Z-scheme mechanism.

In this work, Z-scheme TiO_2-OV-BiOCl with an OVD was prepared according to the following reaction of hydrolysis codeposition at room temperature:

$$2TiCl_3 + NaBiO_3 + 2H_2O \xrightarrow{===} BiOCl(\downarrow) + 2TiO_2(\downarrow) + NaCl + 4HCl \quad (1)$$

The successful preparation of TiO_2-OV-BiOCl composed of BiOCl (001) and TiO_2 (anatase) was demonstrated by SEM, HRTEM, XPS, and XRD. The surfactant F127 is of utmost importance for regulating the OVD in the synthesis of TiO_2/BiOCl, while the OVD mainly exists in 5 layer BiOCl ultrathin nanosheets, as demonstrated by our HRTEM, AFM and XPS analyses. Compared with TiO_2/BiOCl and BiOCl, TiO_2-OV-BiOCl with a rich OVD shows a stronger light utilization, faster photocurrent response, and longer lifetime of the photogenerated charge carriers. These superior characteristics result in a significantly better photocatalytic degradation ability for IMD. The enhancement of photocatalytic activity is attributed to the formation of the Z-scheme heterojunction using the OVD as the charge mediator, which was proved by free radical capture results.

2. Experimental

2.1. Materials

All reagents were of analytical grade and used without further purification. Titanium dioxide (anatase) as control was purchased from Adamas-beta. Imidacloprid (IMD) with 98% purity was provided by the Institute of Plant Protection, Chinese Academy of Agricultural Sciences.

2.2. Synthesis of photocatalysts

1 mmol of sodium bismuthate ($NaBiO_3{\cdot}2H_2O$) was added to a 50 mL methanol solution under stirring for 30 minutes at room temperature to fully disperse it. Titanium trichloride solution (700 μL) was added until $NaBiO_3$ was completely dissolved in the solution which turned from a clear to a pale-yellow solution after 30 min of stirring. This sample was recorded as A solution. The B-labeled solution was composed of an aqueous solution (50 mL) in which 1 g F127 was dissolved completely. The B-labeled solution was added drop by drop to solution A with a peristaltic pump under a slow flow rate of 0.002 mL min^{-1} and stirred for 3 hours to complete the reaction. The resulting precipitation was washed several times with ethanol and water, and dried in a vacuum at 50 °C for 6 hours. The sample obtained is labeled herein as TiO_2-OV-BiOCl. TiO_2/BiOCl as the control was prepared without the addition of F127. In addition, different preparation conditions were also studied since these affect the photocatalytic performance, including different surfactants and solvents, and additive amounts of titanium trichloride solution and the surfactant F127. The BiOCl control samples were prepared the same way as above, except that titanium trichloride solution was replaced by 700 μL of 37% hydrochloric acid.

The type II TiO_2/BiOCl as a control sample was prepared according to a reported procedure in the literature.[25]

2.3. Sample characterization

Powder X-ray diffraction (XRD) measurements were recorded on a Rigaku D/MAX-RB diffractometer with monochromatic Cu Kα radiation (λ = 0.15418 nm). X-ray photoelectron spectra (XPS) were recorded on a VG EscaLab 220i spectrometer, using a standard Al Kα X-ray source (300 W) and an analyzer pass energy of 20 eV. The morphology of the samples was reflected by using a scanning electron microscope (SEM, Hitachi SU8010 Japan) and transmission electron microscope (TEM, Hitachi HT7700 Japan). The morphology of the samples and mapping results were gained from the high resolution TEM (FEI TECNAI G2 F20 200KV American), which was operated at an accelerating voltage of 100 kV. The atomic force microscopy (AFM) measurement was recorded on Digital D3000. The photoluminescence (PL) spectra and time-resolved PL (TRPL) spectra were obtained by using an Edinburgh FLS980 spectrophotometer. 0.2 g of catalyst was used for the specific surface area analysis which was recorded using an N2 adsorption–desorption instrument (BET, ASAP2020, USA). Both the information on oxygen vacancy defects and active species involved in the reaction were determined by using an electron paramagnetic resonance spectrometer (EPR, EMX-8/2.7, Bruker, Germany). The contents of Bi and Ti elements in the catalyst were measured by an inductively coupled plasma optical emission spectrometer (ICP-OES) from PerkinElmer.

2.4. Photocatalytic degradation of IMD in aqueous solution

The photocatalytic degradation of IMD in aqueous solution was studied as follows: 30 mg of photocatalyst was added to 10 ppm of a 50 mL IMD solution. The photocatalyst was fully dispersed in the solution by ultrasonication for 10 minutes and stirring for 30 minutes. These ultrasonication and stirring steps are critical to achieving adsorption–desorption equili-

brium between the photocatalyst and IMD molecules. The photocatalytic degradation of IMD was carried out under a 500 W Xenon lamp (PLS-SXE300, Beijing Changtuo Co. Ltd, Beijing, China), which had a wavelength range from 300 nm to 800 nm with 800 mW cm^{-2} power density. In this experiment, a 3 mL solution was taken out for analysis every 20 minutes. The investigation of photocatalyst stability for IMD degradation was carried out as follows. The photocatalyst used in one degradation cycle was collected by centrifugation, and then it was used again for IMD degradation. This process was repeated five times. The absorbance and concentration of IMD at different degradation times were measured by UV-Vis DRS and UV-HPLC (Agilent semi preparative HPLC, G1322A, C-18 column), with the maximum absorption wavelength of IMD set at 269 nm.

2.5. Photocurrents and electrochemical impedance spectroscopy (EIS)

The photocurrent and EIS data were obtained through an electrochemical workstation (660D, Shanghai Chenhua, China) with a standard three-electrode system (reference electrode (Ag/AgCl (saturated KCl), working electrode and counter electrode (Pt foil)) (1 × 2 cm^2)). ITO glass sheets coated with 1 mg of photocatalyst were used as the working electrode. The detailed preparation process of the working electrode is as follows: 5 mg of catalyst was accurately weighed and placed in a 1.5 mL centrifuge tube, and 1 mL of ethanol solution (50%) was added and ultrasonicated for 30 minutes. 1 mg of photocatalyst of 1 × 1 cm^2 was evenly spread on the ITO glass sheets (1 × 2 cm^2) and then vacuum dried for 4 hours at 80 °C. The electrochemical impedance spectra (EIS) were measured over a frequency range of 10 mHz–1000 kHz with open-circuit voltage. The photocurrent was recorded at −0.64 mV while the simulated sunlight was turned on every 20 seconds.

3. Results and discussion

3.1. Characterization of samples

3.1.1. XRD analysis. The XRD pattern is used to reflect the crystal structure information of samples. As shown in Fig. 1, the prepared BiOCl exhibits the typical BiOCl (001) peak pattern (jade: 06-0249). TiO_2-OV-BiOCl shows characteristic peaks of BiOCl (001) and TiO_2 (anatase), which are consistent with literature reports,[38] indicating the successful integration of a TiO_2/BiOCl heterojunction. TiO_2/BiOCl shows a similar XRD pattern to TiO_2-OV-BiOCl, which implies that the addition of the surfactant F127 does not introduce changes to the crystal structure. To prove the efficiency of "doping" between TiO_2 and BiOCl, the ICP analysis was carried out on Bi and Ti elements in BiOCl/TiO_2 and TiO_2-OV-BiOCl, respectively. The mass fractions of the Bi and Ti elements were 89.29 and 3.55 wt% in TiO_2-OV-BiOCl, and 89.16 and 5.10 wt% in BiOCl/TiO_2, respectively. It can be seen that F127 can slightly regulate the content of TiO_2 in BiOCl/TiO_2, which may be beneficial for the improvement of photocatalytic performance. Moreover, the peak intensity of BiOCl was the highest when TiO_2-OV-BiOCl was prepared by using F127 as the surfactant in other solvents or using other surfactants in methanol. In those cases, only a weak signal from TiO_2 was detected (Fig. S1a and b†). TiO_2/BiOCl, with an optimum ratio of TiO_2 to BiOCl, can be produced when methanol is used as the solvent and F127 or PVP as a surfactant. When Pluronic F127 was used as the template and TCl_3 as the precursor, the Ti^{4+} produced by $TiCl_3$ using $BiNaO_3$ as an oxidant can effectively match the cooperative assembly with Pluronic F127.[39] As a result, uniform spherical F127/TiO_2 oligomer composite micelles could be formed, which would be assembled on the surface of BiOCl. The confinement effect of Pluronic F127 may lead to the generation of less content of TiO_2 in TiO_2-OV-BiOCl compared with BiOCl/TiO_2 without F127 as the template. In addition, the diffraction peak at 25.8° of the BiOCl (101) plane is used to estimate the nanoparticle size by the Debye–Scherrer formula shown in eqn (2):

$$D = k\lambda/(B\cos\theta) \quad (2)$$

where D is the average particle size (nm), k is a constant of 0.943, the wavelength (λ) of X-ray is equal to 0.154056 nm, B is the peak width at half height and q is the angle of the BiOCl (101) diffraction peak. The calculated average particle sizes of the BiOCl nanoparticles on TiO_2-OV-BiOCl and BiOCl/TiO_2 are 21.3 and 20.9 nm, respectively. Due to the low content of TiO_2 in TiO_2/BiOCl and TiO_2-OV-BiOCl, the particle size of TiO_2 cannot be obtained through XRD analysis. Moreover, it can be clearly seen from HRTEM (Fig. 2a) that the average particle size of TiO_2 is 10.36 nm.

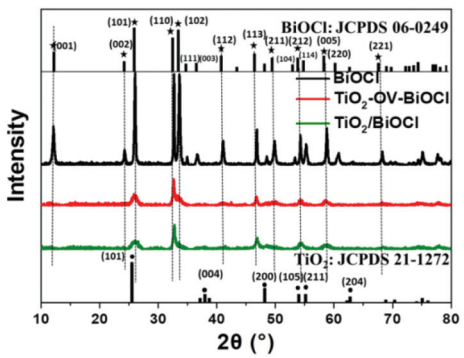

Fig. 1 XRD patterns of TiO_2-OV-BiOCl, TiO_2/BiOCl, and BiOCl.

3.1.2. Morphological observations of the prepared samples. SEM was used to analyze the surface morphology of our samples. TiO_2-OV-BiOCl are assembled as ordered and uniform 3D nanosheets of BiOCl and TiO_2 nanoparticles are attached to the BiOCl surface, as evidenced in Fig. S2a and b.† In contrast, the SEM analysis of TiO_2/BiOCl (Fig. S2c and d†) shows blocky and randomly distributed lamellar structures. The morphology difference between TiO_2-OV-BiOCl and TiO_2/BiOCl is caused by the surfactant F127, which plays a role in regulating the morphology during the synthesis of TiO_2-

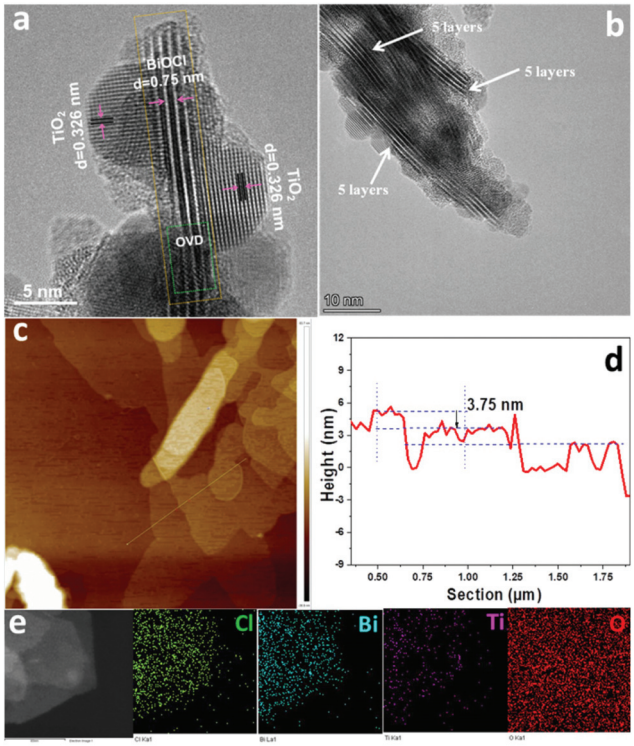

Fig. 2 HRTEM images (a and b), AFM height scans (c) and their corresponding height profiles (d) and the elemental mapping (e) of TiO_2-OV-BiOCl.

OV-BiOCl. The microscopy analysis provides further proof of the successful preparation of TiO_2-OV-BiOCl. As seen in the mapping obtained from HERTEM, the images of Bi and Cl show the same shape, whereas Ti remains localized and all these elements are evenly distributed (Fig. 2e). As can be seen from the HRTEM (Fig. 2a, b and Fig. S2f†) imaging results, the BiOCl nanosheets in TiO_2-OV-BiOCl are composed of five ultrathin layers, each with a thickness of about 0.75 nm. Interestingly, the AFM imaging results also show ultrathin nanosheets with 3.75 nm from TiO_2-OV-BiOCl, which are made up of five ultrathin layers (Fig. 2c and d). Due to their extended and ultrathin 2D nature, these nanosheets are expected to promote the photogenerated charge carrier transfer to the catalyst's surface. Two different *d*-space patterns in HRTEM are shown in Fig. 2a and Fig. S2e,† corresponding to the (112) plane of anatase TiO_2 of 0.326 nm and the (110) plane of tetragonal BiOCl of 0.275 nm, respectively, which are in agreement with the XRD results. Lattice distortion is present due to the oxygen vacancy defects (OVDs), which may mainly exist in BiOCl, as shown in Fig. 2a, Fig. S2e and f.† All in all, the ultrathin layered structure of BiOCl and the intimate contact between TiO_2 and BiOCl are advantageous for the transfer of the photogenerated charges and enhancing the photocatalytic activity.

3.1.3. XPS analysis. XPS characterization was performed to analyze the surface chemical state and elementary composition of the photocatalysts. The survey spectra are shown in Fig. S3a.† The carbon element is detected, which may be introduced by the surfactant F127 remaining in TiO_2-OV-BiOCl. As a semi-quantitative analysis, we deduce from XPS the TiO_2-OV-BiOCl atomic ratios using the peaks Bi 4f, Cl 2p, Ti 2p, and O 1s (12 : 14 : 30 : 25). These values are similar to those of TiO_2/BiOCl (11 : 13 : 31 : 28), indicating that the addition of F127 does not have a considerable effect on the relative atomic composition of TiO_2 and BiOCl. This observation is consistent with the XRD results. Moreover, due to the introduction of an OVD, the O 1s ratio in TiO_2-OV-BiOCl becomes lower than that in TiO_2/BiOCl. Fig. 3a shows the Ti 2p XPS spectrum. The binding energies of TiO_2-OV-BiOCl at 466.1 eV (Ti $2p_{1/2}$) and 458.7 eV (Ti $2p_{3/2}$) belong to Ti^{4+}, and the binding energy of TiO_2-OV-BiOCl at 466.1 eV (Ti $2p_{1/2}$) is almost the same as that of TiO_2/BiOCl, implying that the OVD may not be present in TiO_2. The binding energies of TiO_2-OV-BiOCl at 463.4 eV (Ti $2p_{1/2}$) and 457.9 eV (Ti $2p_{1/2}$) belong to Ti^{3+}. Fig. 3b shows the XPS spectrum for the Bi 4f region. Two characteristic peaks located at 159.15 eV (Bi $4f_{7/2}$) and 164.48 eV (Bi $4f_{5/2}$) in TiO_2-OV-BiOCl belong to Bi^{3+}. No peaks from Bi^{5+} were found, indicating that $NaBiO_3$ is completely reduced to Bi^{3+}. The binding energy of TiO_2-OV-BiOCl at 164.48 eV (Bi $4f_{5/2}$) is 0.28 eV lower than that of TiO_2/BiOCl. This difference may be caused by the introduction of an OVD in BiOCl. Fig. 3c shows the XPS spectrum for O 1s. The binding energies at 530 eV, 531.6 eV, and 532.5 eV belong to those of lattice oxygen, oxygen vacancies, and water molecules adsorbed on the surface of TiO_2-OV-BiOCl, respectively. The binding energy of the oxygen vacancies in TiO_2-OV-BiOCl is 0.7 eV higher than that in TiO_2/BiOCl, which can be attributed to the higher OVD concentration in TiO_2-OV-BiOCl than in TiO_2/BiOCl. The Cl 2p XPS spectrum is shown in Fig. 3d. The binding energies at 197.8 eV and 199.5 eV correspond to Cl $2p_{3/2}$ and Cl $2p_{1/2}$, which are the same as those in BiOCl. All these results demonstrate the successful preparation of the Z-scheme TiO_2-OV-BiOCl, and that

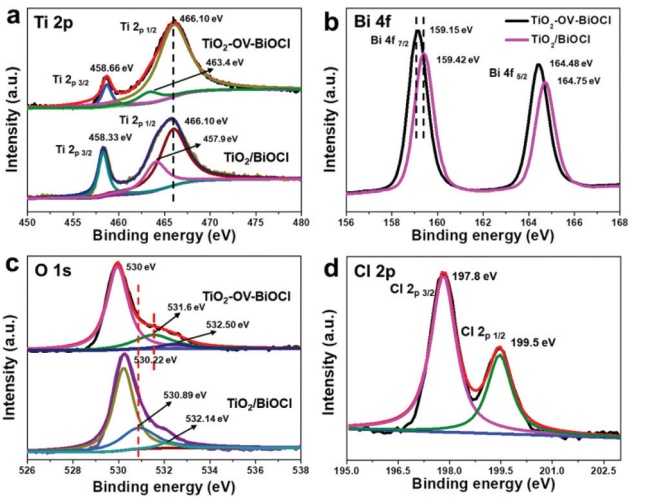

Fig. 3 High-resolution Ti 4f (a), Bi 2p (b) and O 1s (c) XPS spectra of TiO_2-OV-BiOCl and TiO_2/BiOCl and Cl 2p (d) XPS spectra of TiO_2-OV-BiOCl.

the addition of F127 can introduce a higher concentration of OVDs in BiOCl in the synthesis of TiO_2/BiOCl.

3.1.4. UV/Vis DRS and EPR analyses. UV/Vis DRS and EPR (electron paramagnetic resonance) analyses were used to characterize light absorption and surface defects of samples. The light absorption is critical to photocatalytic performance. In general, a wide absorption spectrum corresponds to excellent photocatalytic degradation properties. According to UV/Vis DRS results (Fig. 4a), at the absorption edge, TiO_2-OV-BiOCl shows a more pronounced redshift and higher light absorption than BiOCl and TiO_2/BiOCl, which is mainly attributed to the formation of a Z-scheme heterojunction of TiO_2-OV-BiOCl. As shown in the EPR spectrum (Fig. 4b), the oxygen vacancies' signal is detected at g = 2.004 in TiO_2/BiOCl and TiO_2-OV-BiOCl. TiO_2-OV-BiOCl shows a stronger signal intensity than TiO_2/BiOCl, which implies that the addition of F127 can introduce a higher concentration of OVDs in the synthesis of TiO_2/BiOCl, which is consistent with the XPS results. The successful introduction of OVDs may result in increased light absorption. The possible reasons why surfactants can introduce oxygen vacancy defects are as follows:[40,41] during the nucleation process, the "–C═O" in the F127 unit may prefer to interact with the unsaturated and positively charged Bi atoms on the BiOCl surface in order to reduce the surface energy, leading to the generation of abundant oxygen vacancies.

3.1.5. Photocurrent response, EIS, and the steady-state PL, TRPL spectra and surface photovoltage (SPV) spectroscopy. Photocurrent response and electrochemical impedance spectroscopy (EIS) experiments were performed to study the effect of OVDs in Z-scheme TiO_2/BiOCl regulated by F127 for the separation and transfer of the photogenerated charge carriers. The TiO_2-OV-BiOCl photocatalyst shows a remarkably higher photocurrent density than TiO_2/BiOCl and BiOCl, as shown in Fig. 5a. This result can be understood by considering that TiO_2-OV-BiOCl has a higher separation and migration efficiency of the photogenerated charges than TiO_2/BiOCl and BiOCl. The EIS in Fig. 5b shows TiO_2-OV-BiOCl with a smaller semicircle in the Nyquist plots than TiO_2/BiOCl and BiOCl under both dark and light conditions. This observation implies that TiO_2-OV-BiOCl has a faster proton migration rate than TiO_2/BiOCl and BiOCl. The steady-state PL spectra are used to indicate the effect of OVDs on the lifetime of the photogenerated electrons (Fig. 5c), where the peak intensity of TiO_2-OV-BiOCl appears

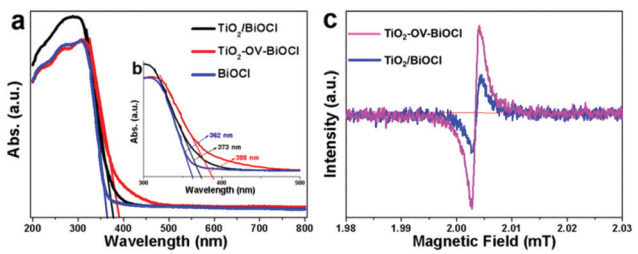

Fig. 4 (a) UV/Vis DRS for TiO_2-OV-BiOCl, TiO_2/BiOCl and BiOCl and (b) an enlarged inset ranging from a 300 to 500 nm wavelength; (c) The EPR analysis for TiO_2-OV-BiOCl, TiO_2/BiOCl.

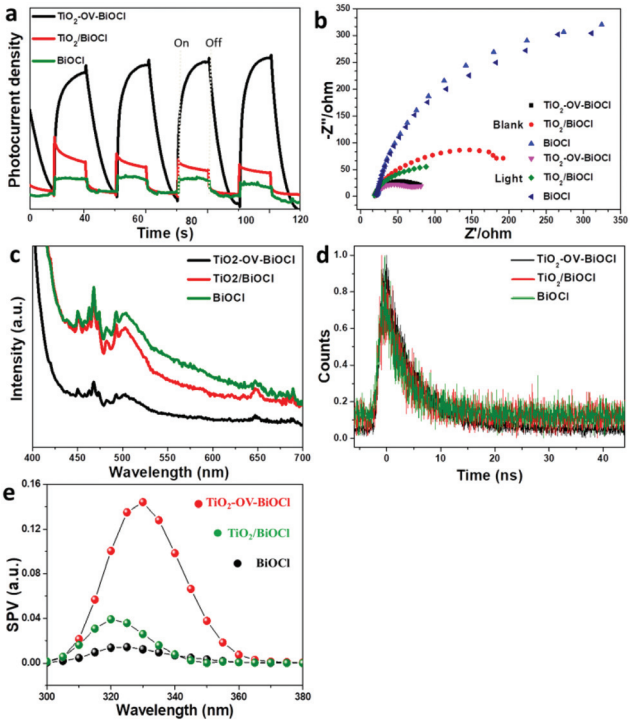

Fig. 5 The photocurrent response (a) and the electrochemical impedance spectroscopy (EIS) (b) for TiO_2-OV-BiOCl, TiO_2/BiOCl and BiOCl; The steady-state PL spectra (c) and TRPL spectra (d) for TiO_2-OV-BiOCl, TiO_2/BiOCl and BiOCl; Surface photovoltage (SPV) spectroscopy on TiO_2-OV-BiOCl, TiO_2/BiOCl and BiOCl.

lower than those of TiO_2/BiOCl and BiOCl. Thus we can infer that the photogenerated charges in TiO_2-OV-BiOCl are driven to separate and thus show a lower fluorescence due to a lower recombination, supporting a prolonged lifetime of the photogenerated electrons. Moreover, the TRPL spectra are used to investigate the effects of OVDs on the lifetime of the photogenerated electrons (Fig. 5d). The intensity-averaged lifetime (τ_m = 5.83 ns) of TiO_2-OV-BiOCl is prominently longer than the corresponding values for TiO_2/BiOCl (τ_m = 4.76 ns) and BiOCl (τ_m = 4.33 ns). The calculation process of the intensity-average lifetime of samples is presented in detail in the ESI.† The average lifetime of electrons in TiO_2-OV-BiOCl deduced from PL spectra is lengthened, which may be attributed to the formation of the Z-scheme heterojunction of TiO_2-OV-BiOCl where the OVD acts as a charge mediator. To further understand the role of the OVD, we measured the surface photovoltage (SPV) of the samples. Fig. 5e exhibits that the intensity of SPV on TiO_2-OV-BiOCl is obviously stronger than those of TiO_2/BiOCl and BiOCl. Therefore, all these results confirm that OVDs as charge mediators can promote the transport, separation, and lifetime of photogenerated charge carriers, characteristics that are responsible for ensuring an excellent degradation performance.

3.2. Photocatalytic degradation for IMD performance

The photocatalytic performance was evaluated by the photocatalytic degradation of IMD under simulated sunlight. Fig. 6a

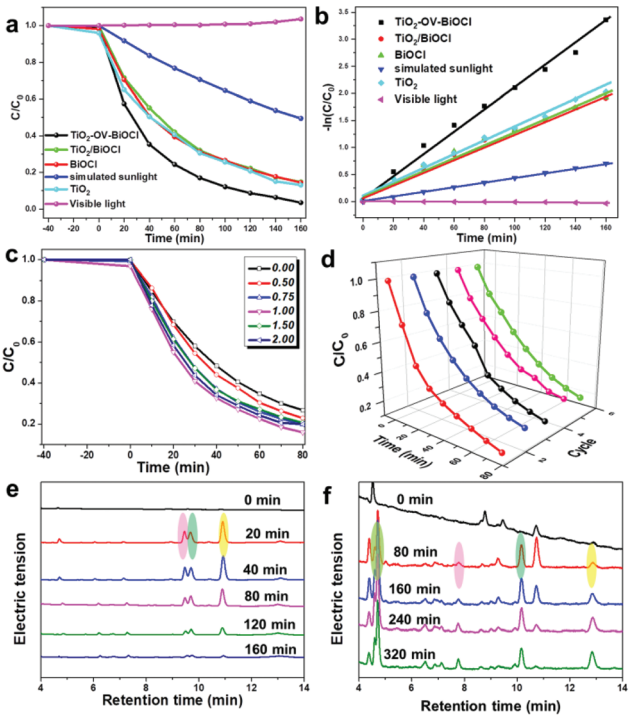

Fig. 6 Photocatalytic degradation courses of IMD over TiO_2-OV-BiOCl, TiO_2/BiOCl, BiOCl and TiO_2 and photo-degradation by simulated sunlight and visible light (a) and the corresponding pseudo-first order kinetics plots (b); photocatalytic degradation courses of IMD over TiO_2-OV-BiOCl under different additive amounts of F127 (0–2 g) (c); photocatalytic degradation of IMD courses in the repeated tests over TiO2-OV-BiOCl (d); HPLC graphs of by-products within the same retention times undergoing photocatalytic degradation over TiO_2-OV-BiOCl (e) and photo-degradation by simulated sunlight (f).

and b show that IMD is not adsorbed by the photocatalyst and exhibits only a minor degradation without any photocatalyst under illumination. Therefore, the adsorption of IMD can be ignored and the decreased concentration of IMD is mainly attributed to photocatalysis and photo-degradation. Compared with BiOCl, TiO_2/BiOCl, and TiO_2, the TiO_2-OV-BiOCl photocatalyst displays the best photocatalytic degradation performance. We attribute this superior performance to the introduction of an OVD in BiOCl, which constructs the Z-scheme heterojunction as a charge mediator in TiO_2-OV-BiOCl, promoting the separation, transport, and lifetime of the photogenerated charges and enhancing light absorptivity. The photocatalyst BET is one of the important factors affecting photocatalytic degradation activity, and thus it is closely related to photocatalytic degradation performance. As can be seen from Fig. S3b,† the prepared TiO_2-OV-BiOCl exhibits a large BET (93.9816 $m^2\ g^{-1}$) that promotes the photocatalytic degradation of IMD. However, the BET of TiO_2/BiOCl (138.8673 $m^2\ g^{-1}$) is larger than that of TiO_2-OV-BiOCl. Thus, in this case, the superior photocatalytic performance of TiO_2-OV-BiOCl should be mainly attributed to the formation of the Z-scheme heterojunction using the OVD as a charge mediator rather than the photocatalyst's BET. To investigate this further, different amounts of F127 were studied to reveal the effect of this surfactant in the synthesis of TiO_2-OV-BiOCl and the photocatalytic degradation performance. The photocatalytic degradation of IMD accelerates with the increase in F127 content, which is mainly attributed to the regulation of the OVD in TiO_2/BiOCl, as evidenced by the results in Fig. 6c. However, the photocatalytic degradation is suppressed when the additive amount of F127 is more than one gram. This photocatalysis suppression is due to excessive F127 in TiO_2/BiOCl that inhibits the photocatalytic activity. A large number of experimental conditions were considered for screening out the best photocatalyst for the degradation of IMD. It is important to carefully account for experimental conditions since they affect the photocatalytic properties, including different solvent systems, types of surfactant and the addition of titanium trichloride solution (Fig. S4a–c†). When F127 or PVP is used as a surfactant in a methanol solvent, TiO_2-OV-BiOCl will be formed, showing an excellent photocatalytic activity. However, the photocatalytic degradation activity becomes weaker when TiO_2-OV-BiOCl is prepared by using F127 as the surfactant in other solvents or using other surfactants in methanol. This result is due to the formation of only a small amount of TiO_2 in the composition of TiO_2/BiOCl according to the XRD results (see Fig. S1a and b†). Photocatalyst stability is a very important parameter for evaluating the photocatalyst performance and service life. Fig. 6d shows that TiO_2-OV-BiOCl still has good degradation activity after five degradation cycles. This stability may be attributed to the formation of the Z-scheme heterojunction of TiO_2-OV-BiOCl and the minimized photocorrosion of BiOCl. However, the photocorrosion of BiOCl occurs after one cycle of degradation and the color of BiOCl changes from white to black (Fig. S4d†), where bismuth ions (Bi^{3+}) are easily reduced to metallic bismuth.[42–44] In short, the Z-scheme heterojunction of TiO_2-OV-BiOCl using the OVD as a charge mediator not only promotes photocatalytic degradation activity, but also increases the stability of TiO_2-OV-BiOCl. HPLC was used to reflect the degradation processes of IMD and evaluate degradation performance. The photocatalytic degradation of IMD (10 ppm) could reach 97% in 160 min under light, and four intermediates were detected at about 9.45, 9.7, 10.92 and 19 min. These by-products accumulate gradually with the increase of the reaction time, reaching the highest level at 40 min under illumination. After this time, the reaction begins to decrease. These results are presented in Fig. 6e and Fig. S5a.† When the photocatalytic degradation time reached 160 min, IMD and its four intermediates were basically degraded, showing that TiO_2-OV-BiOCl has an excellent degradation ability for IMD. The four intermediates formed during the photocatalytic degradation of IMD over TiO_2-OV-BiOCl were analyzed by LC/MS. The iron spectra at different retention times of photocatalytic degradation for IMD under irradiation at 40 min are recorded in the ESI Scan (Fig. S6†). Based on the LC-MS/TOF results, we identify the molecular structures of four intermediates and propose a most likely photocatalytic degradation pathway of IMD (Scheme 1). However, it can be seen from Fig. 6f and Fig. S5b–d† that IMD

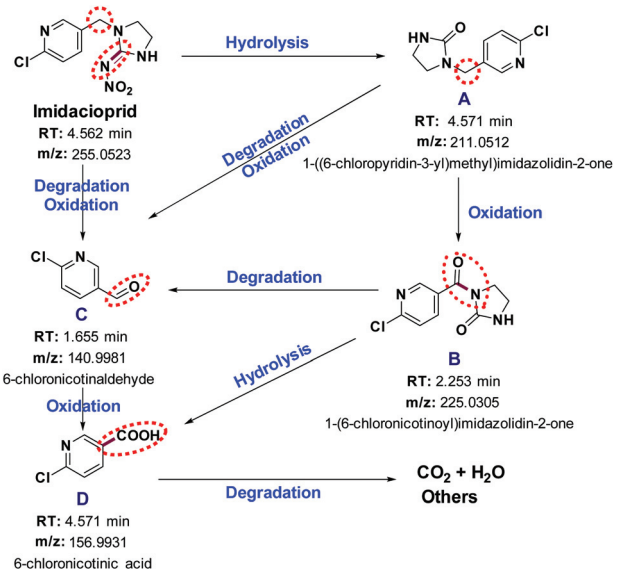

Scheme 1 A possible degradation pathway of IMD.

cannot be degraded in visible light and can be only partially degraded after 360 min in simulated sunlight without any photocatalyst. Yet, the by-products follow the opposite trend, showing that the photo-degradation is only the conversion of IMD into the intermediate products that are more difficult to degrade.

3.2.1. Free radical trapping experiments. Free radical capture experiments and EPR characterization were carried out to study the main active species involved in the degradation of IMD under simulated sunlight. Fig. 7a shows results from these experiments. Sodium oxalate (SO), as an effective hole scavenger, inhibits the photocatalytic degradation of IMD, indicating that holes (h^+) are directly involved in the reaction. Nitrogen bubbling is used to illustrate the effect of superoxide radicals ($^{\bullet}O_2^-$) preformed by removing dissolved oxygen initially present in solution. This oxygen removal significantly suppresses IMD degradation, suggesting that superoxide radicals ($^{\bullet}O_2^-$) are the active species driving IMD degradation. This conclusion is supported by EPR results where the signal of the superoxide radicals ($^{\bullet}O_2^-$) increases with the extended illumination time in simulated sunlight (Fig. 7b). In contrast, isopropanol (IPA), as a scavenger of the hydroxyl radicals ($^{\bullet}OH$), has no significant effect on IMD photocatalytic degradation, implying that hydroxyl radicals ($^{\bullet}OH$) are not the main species involved in the reaction. However, a signal of the hydroxyl radicals ($^{\bullet}OH$) can also be detected in EPR (Fig. 7c), which may be due to the presence of type II heterojunctions in TiO_2-OV-BiOCl. In summary, we found that the main active species involved in IMD degradation are holes (h^+) and superoxide radicals ($^{\bullet}O_2^-$).

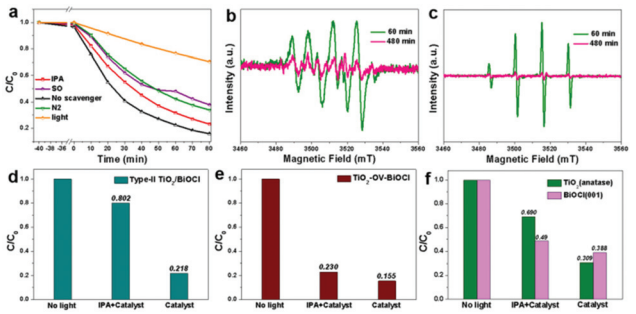

Fig. 7 The effects of various scavengers on the photocatalytic degradation of IMD using TiO_2-OV-BiOCl (a); the ESR spectra of (b) DMPO-$^{\bullet}O_2^-$ and (c) DMPO-$^{\bullet}OH$ by TiO_2-OV-BiOCl; the effects of the hydroxyl radicals on the photocatalytic degradation of IMD using type-II TiO_2/BiOCl (d), Z-scheme TiO_2-OV-BiOCl (e), TiO_2(anatase) and BiOCl (001) (f) of illumination for 80 minutes.

3.2.2. Photocatalytic degradation mechanism. The photocatalytic oxidative degradation of TiO_2 is mainly attributed to hydroxyl radicals that stem from the oxidation of H_2O by holes,[45–48] as shown in Fig. 6f, while that of BiOCl is mainly caused by the direct oxidation of holes.[49–51] When the TiO_2/BiOCl heterojunction is formed, the charge-transfer mode is known as the type-II mechanism.[20–25] The main free radicals for photocatalytic degradation are superoxide radicals ($^{\bullet}O_2^-$) produced at the CB of BiOCl and hydroxyl radicals ($^{\bullet}OH$) produced at the VB of TiO_2. The photocatalytic degradation activity of IMD by type II TiO_2/BiOCl was inhibited when 5 mmol of isopropanol (IPA) as a hydroxyl radical ($^{\bullet}OH$) scavenger was added to an IMD solution, as shown in Fig. 7d. This result proves that hydroxyl radicals ($^{\bullet}OH$) produced at the VB of TiO_2 are the main free radicals in the oxidation of type II TiO_2/BiOCl. The IPA as a hydroxyl radical ($^{\bullet}OH$) scavenger has little effect on the photocatalytic degradation of IMD when TiO_2-OV-BiOCl is used as the photocatalyst, see Fig. 7e. However, the SO can inhibit the photocatalytic degradation of IMD (Fig. 7a), indicating that the hole (h^+) produced at the VB of BiOCl is the main active species rather than the hydroxyl radical ($^{\bullet}OH$) produced at the VB of TiO_2 for IMD photocatalytic degradation. Our results are in agreement with the work of Zhou *et al.*, who reported that the photocatalytic degradation of TiO_2/BiOCl with a rich OVD was caused by holes (h^+) rather than superoxide radicals ($^{\bullet}OH$).[52] Similar results have been reported in other TiO_2/BiOCl,[38,53] possibly due to the introduction of oxygen vacancy defects in TiO_2/BiOCl. The above analysis shows that, when the OVD is introduced into the TiO_2-OV-BiOCl heterojunction, the OVD as a 'charge mediator' may lead to the construction of a Z-scheme heterojunction where the charge-transfer mode may change from type-II to Z-type mechanism. The photocatalytic degradation mechanism of type-II and Z-scheme TiO_2/BiOCl is shown in Scheme 1. The VB and CB of TiO_2 and BiOCl are illustrated according to reported literature values.[21,23,25,53] Unlike the type-II mechanism, the Z-scheme mechanism not only possesses the advantages of the type-II mechanism but also maintains strong redox potentials. This gives rise to an effective strategy to promote photocatalytic degradation performance. The charge-transfer mode of TiO_2/BiOCl without the addition of F127 is mainly based on the type-II mechanism. As illustrated in Fig. 4a, 5 and 6a, although the photocatalyst TiO_2/BiOCl shows

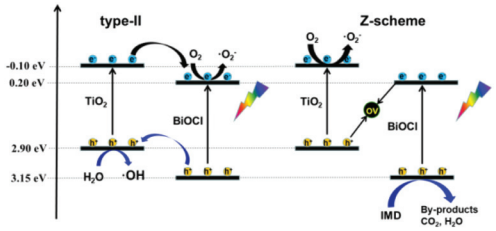

Scheme 2 A plausible photocatalytic degradation mechanism of type-II and Z-scheme TiO_2/BiOCl.

higher light absorption and separation efficiency of photogenerated charge carriers with a longer lifetime than BiOCl, it does not show better IMD degradation activity than BiOCl. This difference is attributed to a weaker redox potential of TiO_2/BiOCl. TiO_2-OV-BiOCl with a rich OVD as a charge mediator may be mainly based on the Z-scheme mechanism, which remarkably exhibits excellent light absorption, in addition to a better separation, migration, and lifetime of the photogenerated charge carriers. These characteristics, in addition to its stronger redox ability, give the rich-OVD-based TiO_2-OV-BiOCl a better degradation activity than TiO_2/BiOCl and BiOCl (Scheme 2).

4. Conclusion

In summary, a novel Z-scheme TiO_2/BiOCl with a rich OVD is successfully developed. The XPS, HRTEM, EPR, and UV/Vis DRS results show the introduction of a rich OVD in TiO_2-OV-BiOCl. This addition extends the light absorption range of the photocatalyst. Photoelectrochemical analysis and PL/TRPL spectra prove that the formation of a Z-scheme heterojunction in TiO_2/BiOCl with a rich OVD promotes the separation efficiency and prolonged lifetime of the photogenerated charges, supporting an excellent degradation ability for IMD. The OVD as a charge mediator may lead to a charge-transfer mode change from type II to a Z-scheme mechanism. This interpretation is confirmed by free radical capture experiments. The prepared TiO_2-OV-BiOCl photocatalyst shows an excellent degradation ability for IMD and a possible degradation pathway of IMD was proposed in combination with HPLC and LC-MS. In short, a Z-scheme heterojunction with TiO_2/BiOCl was developed by using the OVD as a charge mediator. This heterostructure can be applied to efficient photocatalytic degradation of pesticides.

Conflicts of interest

There are no conflicts to declare.

Acknowledgements

This study was supported by the National Natural Science Foundation of China (U1703351, 51663021), Bingtuan Excellent Young Scholars (CZ027205) and Bingtuan Science & Technology Nova Program. We wish to thank the Analysis and Testing Center of Shihezi University for the microscopy and microanalysis of our specimens.

References

1 W. Hayat, Y. Zhang, I. Hussain, X. Du, M. Du, C. Yao, S. Huang and F. Si, *Chem. Eng. J.*, 2019, **370**, 1169–1180.
2 G. Rózsa, M. Náfrádi, T. Alapi, K. Schrantz, L. Szabó, L. Wojnárovits, E. Takács and A. Tungler, *Appl. Catal., B*, 2019, **250**, 429–439.
3 C. K. Remucala, *Environ. Sci.: Processes Impacts*, 2014, **16**, 628–653.
4 V. Kitsiou, N. Filippidis, D. Mantzavinos and I. Poulios, *Appl. Catal., B*, 2009, **86**, 27–35.
5 B. Tang, H. Shi, Z. Fan and G. Zhao, *Chem. Eng. J.*, 2018, **334**, 882–890.
6 M. Bourgin, F. Violleau, L. Debrauwer and J. Albet, *J. Hazard. Mater.*, 2011, **190**, 60–68.
7 J. Yan, Y. Chen, W. Gao, Y. Chen, L. Qian and L. Han, *Chemosphere*, 2019, **225**, 157–165.
8 Y. Aimer, O. Benali and K. G. Serrano, *Sep. Purif. Technol.*, 2019, **208**, 27–33.
9 X. Chen, X. Xue and X. Gong, *Dalton Trans.*, 2020, **49**, 5205–5218.
10 B. Yang, Z. Ma, Q. Li, X. Liu, Z. Liu, W. Yang, X. Guo and X. Jia, *New J. Chem.*, 2020, **44**, 1090–1096.
11 C. M. Batikian, A. Lu, K. Watanabe, J. Pitt and R. M. Gersberg, *Chemosphere*, 2019, **223**, 83–90.
12 W. Liu, Y. Shang, A. Zhu, P. Tan, Y. Liu, L. Qiao, D. Chu, X. Xiong and J. Pan, *J. Mater. Chem. A*, 2017, **5**, 12542–12549.
13 L. Liu, Y. Sun, X. Cui, K. Qi, X. He, Q. Bao, W. Ma, J. Lu, H. Fang, P. Zhang, L. Zheng, L. Yu, D. J. Singh, Q. Xiong, L. Zhang and W. Zheng, *Nat. Commun.*, 2019, **10**, 4472.
14 J. Liu, S. Zhang and H. Zhao, *Appl. Surf. Sci.*, 2019, **479**, 247–252.
15 H. Wang, W. Zhang, X. Li, J. Li, W. Cen, Q. Li and F. Dong, *Appl. Catal. B: Environ.*, 2018, **225**, 218–227.
16 J. Li, L. Cai, J. Shang, Y. Yu and L. Zhang, *Adv. Mater.*, 2016, **28**(21), 4059–4064.
17 J. Hu, X. Li, X. Wang, Q. Lia and F. Wang, *Dalton Trans.*, 2019, **48**, 8937–8947.
18 Q. Wang, W. Wang, L. Zhong, D. Liu, X. Cao and F. Cui, *Appl. Catal., B*, 2018, **220**, 290–302.
19 L. Lei, H. Jin, Q. Zhang, J. Xu, D. Gao and Z. Fu, *Dalton Trans.*, 2015, **44**, 795–803.
20 M. Guerrero, A. Altube, E. García-Lecina, E. Rossinyol, M. D. Baró, E. Pellicer and J. Sort, *ACS Appl. Mater. Interfaces*, 2014, **16**, 13994–14000.
21 D. Sánchez-Rodríguez, M. G. M. Medrano, H. Remita and V. Escobar-Barrios, *J. Environ. Chem. Eng.*, 2018, **6**, 1601–1612.
22 Q. Wang, P. Li, Z. Zhang, C. Jiang, K. Zuo, J. Liu and Y. Wang, *J. Photochem. Photobiol., A*, 2019, **378**, 114–124.

23 F. Duo, Y. Wang, C. Fan, X. Mao, X. Zhang, Y. Wang and J. Liu, *Mater. Charact.*, 2015, **99**, 8–16.
24 K. Wang, C. Shao, X. Li, X. Zhang, N. Lu, F. Miao and Y. Liu, *Catal. Commun.*, 2015, **67**, 6–10.
25 D. Sun, J. Li, L. He, B. Zhao, T. Wang, R. Li, S. Yin, Z. Feng and T. Sato, *CrystEngComm*, 2014, **16**, 7564–7574.
26 W. Ouyang, F. Teng and X. Fang, *Adv. Funct. Mater.*, 2018, 1707178.
27 L. Zhu, H. Li, P. Xia, Z. Liu and D. Xiong, *ACS Appl. Mater. Interfaces*, 2018, **46**, 39679–39687.
28 Z. Jiao, X. Guan, M. Wang, Q. Wang, B. Xu, Y. Bi and X. Zhao, *Chem. Eng. J.*, 2019, **356**, 781–790.
29 Q. Ma, X. Peng, M. Zhu, X. Wang, Y. Wang and H. Wang, *Electrochem. Commun.*, 2018, **95**, 28–32.
30 X. Wen, C. Niu, L. Zhang, C. Liang, H. Guo and G. Zeng, *J. Catal.*, 2018, **358**, 141–154.
31 R. Wang, G. Qiu, Y. Xiao, X. Tao, W. Peng and B. Li, *J. Catal.*, 2019, **374**, 378–390.
32 Q. A. Drmosh, A. Hezam, A. H. Y. Hendi, M. Qamar, Z. H. Yamani and K. Byrappa, *Appl. Surf. Sci.*, 2020, **499**, 143938.
33 X. Li, H. Shi, T. Wang, Y. Zhang, S. Zuo, S. Luo and C. Yao, *Appl. Surf. Sci.*, 2018, **456**, 835–844.
34 Y. Pang, Y. Li, G. Xu, Y. Hu, Z. Kou, Q. Feng, J. Lv, Y. Zhang, J. Wang and Y. Wu, *Appl. Catal., B*, 2019, **248**, 255–263.
35 H. Gao, R. Cao, X. Xu, S. Zhang, Y. Huang, H. Yang, X. Deng and J. Li, *Appl. Catal., B*, 2019, **245**, 399–409.
36 J. Ding, Z. Dai, F. Qin, H. Zhao, S. Zhao and R. Chen, *Appl. Catal., B*, 2017, **205**, 281–291.
37 X. Gao, G. Tang, W. Peng, Q. Guo and Y. Luo, *Chem. Eng. J.*, 2019, **360**, 1320–1329.
38 W. Li, Y. Tian, H. Li, C. Zhao, B. Zhang, H. Zhang, W. Geng and Q. Zhang, *Appl. Catal., A*, 2016, **516**, 81–89.
39 W. Zhang, H. He, Y. Tian, K. Lan, Q. Liu, C. Wang, Y. Liu, A. Elzatahry, R. Che, W. Li and D. Zhao, *Chem. Sci.*, 2019, **10**, 1664–1670.
40 X. Xue, R. Chen, H. Chen, Y. Hu, Q. Ding, Z. Liu, L. Ma, G. Zhu, W. Zhang, Q. Yu, J. Liu, J. Ma and Z. Jin, *Nano Lett.*, 2018, **18**(11), 7372–7377.
41 G. Zhang, Z. Hu, M. Sun, Y. Liu, L. Liu, H. Liu, C. Huang, J. Qu and J. Li, *Adv. Funct. Mater.*, 2015, **24**, 3726–3734.
42 S. Weng, B. Chen, L. Xie, Z. Zheng and P. Liu, *J. Mater. Chem. A*, 2013, **1**, 3068.
43 F. Dong, T. Xiong, S. Yan, H. Wang, Y. Sun, Y. Zhang, H. Huang and Z. Wu, *J. Catal.*, 2016, **344**, 401–410.
44 H. Wang, W. Zhang, X. Lia, J. Li, W. Cen, Q. Lia and F. Dong, *Appl. Catal., B*, 2018, **225**, 218–227.
45 S. Wu, J. Sun, S. Yang, Q. He, L. Zhang and L. Sun, *Inorg. Chem.*, 2018, **57**, 8988–8993.
46 X. Hu, X. Hu, Q. Peng, L. Zhou, X. Tan, L. Jiang, C. Tang, H. Wang, S. Liu, Y. Wang and Z. Ning, *Chem. Eng. J.*, 2020, **380**, 122366.
47 J. Zhong, Y. Zhao, L. Ding, H. Ji, W. Ma, C. Chen and J. Zhao, *Appl. Catal., B*, 2019, **241**, 514–520.
48 W. Dong, Y. Yao, L. Li, Y. Sun, W. Hua, G. Zhuang, D. Zhao, S. Yan and W. Song, *Appl. Catal., B*, 2017, **217**, 293–302.
49 R. B. Arthur, J. L. Bonin, L. P. Ardill, E. J. Rourk and H. H. Patterson, *J. Hazard. Mater.*, 2018, **358**, 1–9.
50 X. Gao, W. Peng, G. Tang, Q. Guo and Y. Luo, *J. Alloys Compd.*, 2018, **757**, 455–465.
51 X. Gao, Q. Guo, G. Tang, W. Zhu and Y. Luo, *J. Solid State Chem.*, 2019, **277**, 133–138.
52 S. Zhou, N. Bao, Q. Zhang, X. Jie and Y. Jin, *Appl. Surf. Sci.*, 2019, **471**, 96–107.
53 X. Hu, Z. Sun, J. Song, G. Zhang, C. Li and S. Zheng, *J. Colloid Interface Sci.*, 2019, **533**, 238–250.